In-Plane Porous Graphene: A Promising Anode Material with High Ion Mobility and Energy Storage for Rubidium-Ion Batteries

Baichuan Lu, Ning Ru, Junyi Duan, Zesheng Li, and Jifeng Qu*

Read Online

ACCESS | Metrics & More | Article Recommendations | Supporting Information

ABSTRACT: Rubidium-ion batteries (RIBs) have received a lot of attention in the quantum field because of their fast release and reversible advantages as alkali sources. However, the anode material of RIBs still follows graphite, whose layer spacing can greatly restrict the diffusion and storage capability of Rb-ions, posing a significant barrier to RIB development. Herein, using first-principles calculations, the potential performance of three kinds of in-plane porous graphene with pore sizes of 5.88 Å (HG588), 10.39 Å (HG1039), and 14.20 Å (HG1420) as anode materials for RIBs was explored. The results indicate that HG1039 appears to be an appropriate anode material for RIBs. HG1039 has excellent thermodynamic stability and a volume expansion of <25% during charge and discharge. The theoretical capacity of HG1039 is up to 1810 mA h g^{-1}, which is ~5 times higher than that of the existing graphite-based lithium-ion batteries. Importantly, not only HG1039 enables the diffusion of Rb-ions at the three-dimensional level but also the electrode−electrolyte interface formed by HG1039 and Rb-β-Al_2O_3 facilitates the arrangement and transfer of Rb-ions. In addition, HG1039 is metallic, and its outstanding ionic conductivity (diffusion energy barrier of only 0.04 eV) and electronic conductivity indicates superior rate capability. These characteristics make HG1039 an appealing anode material for RIBs.
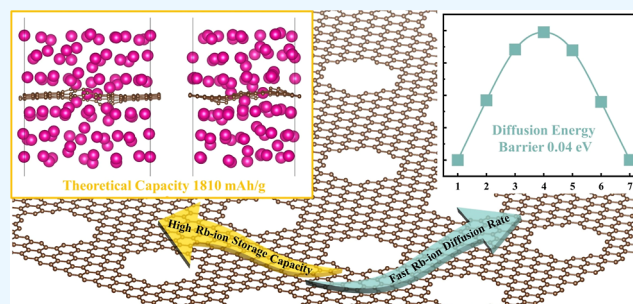
1. INTRODUCTION

After decades of continuous development, the technology of electrochemical storage alkali metals represented by lithium-ion batteries (LIBs) is being widely used in modern society with its high charge−discharge efficiency and long-term cycle stability.[1−3] However, due to the scarcity and uneven distribution of lithium resources, researchers have shifted their attention to other alkali-based electrochemical energy-storage devices, such as sodium-ion batteries (SIBs) and potassium-ion batteries, which share the ion rocking-chair operating mechanism with LIBs.[4−6] Also, being an alkali metal, rubidium-ion (Rb-ion) batteries (RIBs) appear to be very promising and worth investigating; their potential advantages include (1) the diffusion coefficient and mobility of alkali cations usually increase with increasing atomic number,[7] and the weaker Lewis acidity of the Rb-ion (smaller solvated ions) gives rise to higher ionic conductivity than the Li-ion, Na-ion, and K-ion.[8] (2) The standard redox potential of Rb^+/Rb (−2.98 V vs SHE) in the electrolyte is very similar to that of Li^+/Li (−3.04 V vs SHE), allowing higher cell voltages to be maintained.[9] (3) Rb's crustal reserves are richer than Li. All aforementioned characteristics bode well for the development of RIBs as promising battery systems. Biby et al. reported that the theoretical quantum capacity of the Rb-ion supercapacitor using MoS_2 as the electrode material can reach 3300 F/g.[10] Our previous work has revealed that RIBs using monolayer MoS_2 anode materials not only have comparable theoretical

capacities but also have approximately one order of magnitude lower diffusion energy barriers compared to commercial LIBs (graphite anodes).[11] Recently, McGilligan and Kang disclosed RIBs that can be utilized as a Rb-atom source.[12−15] Their advantages of being fast and having a low power, high purity, small size, and reversibility make them one of the key technologies for the development of quantum fields, such as miniaturized cold/ultra-cold atom physics systems, efficient photon−photon logic gates, and efficient quantum memories.[16−18]

Despite their enormous promise, RIBs are in their infancy, with high-performance electrode materials and scientific challenges yet to be discovered and overcome. A major obstacle limiting the performance of RIBs is the anode material because the existing one still follows the commercial LIBs (i.e., graphite anode). Although graphite has excellent specific capacity for storing Li, the results of both Na and K storage, when it is utilized as the active material for the anode, are not satisfactory. This is primarily caused by the large ionic radii of
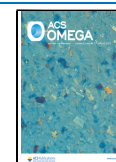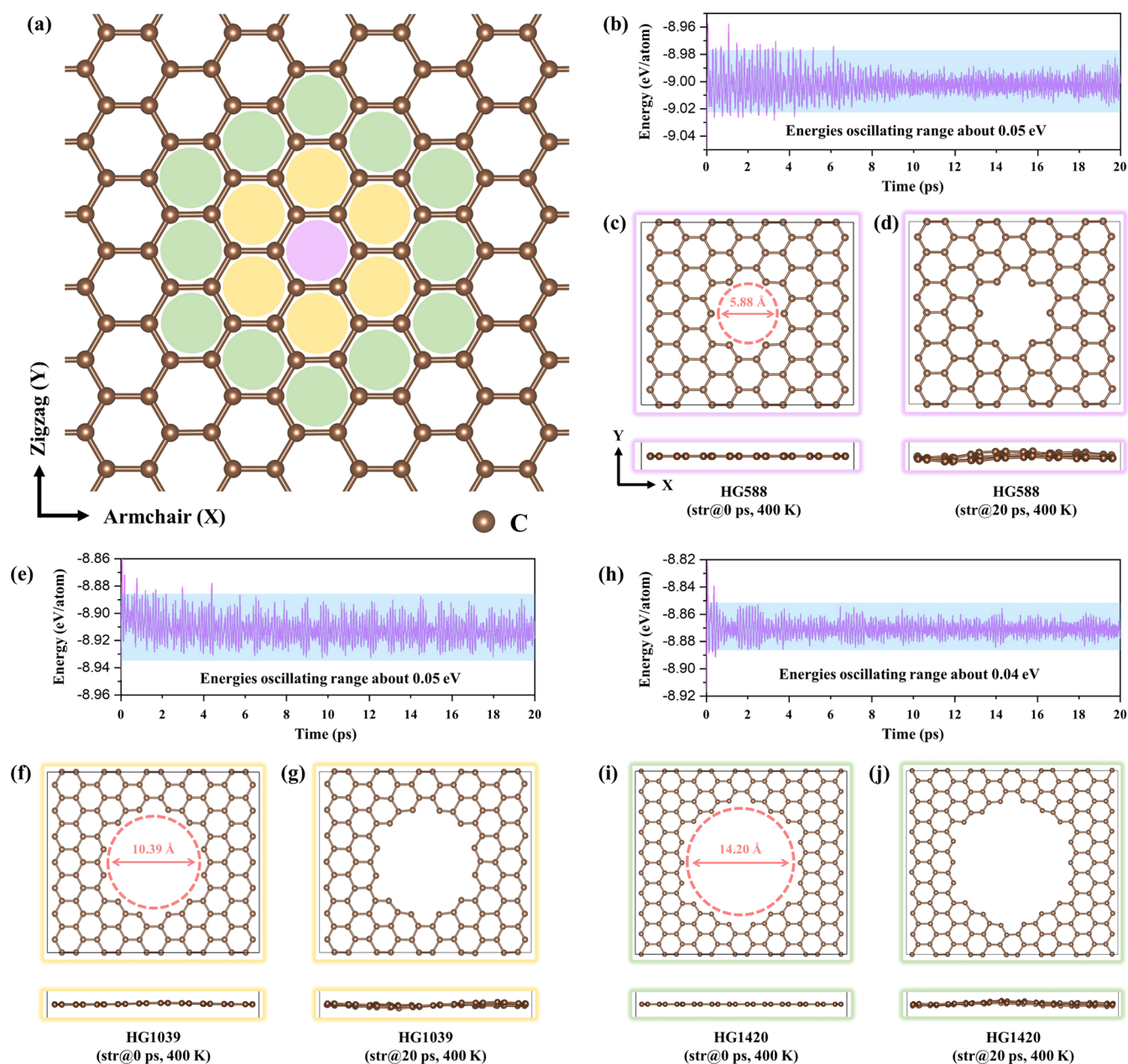
Figure 1. (a) Schematic diagram of an equilateral hexagonal defect based on graphene with an orthogonal lattice. The pink, yellow, and green defect structures indicate the HG588, HG1039, and HG1420 systems, respectively. The evolution of total energy per atom of (b) HG588, (e) HG1039, and (h) HG1420 is obtained from 20 ps AIMD simulations at 400 K. The geometrically optimized (c) HG588, (f) HG1039, and (i) HG1420 structures are the starting configurations (i.e., str@0 ps). The final configurations of (d) HG588, (g) HG1039, and (j) HG1420 at t = 20 ps (i.e. str@20 ps).

Na and K, which hinder the ion intercalation/deintercalation during the charging/discharging process and also leads to a disorder in the long-term cycle of the graphite structure.[19] The radius of Rb is larger than those of Na and K and severely mismatches the graphite layer spacing of 3.35 Å. When a significant quantity of Rb-ion is intercalated/deintercalated to graphite, this can worsen the material's instability and quickly cause a number of issues, including low capacity, poor cyclability, and low initial Coulombic efficiency. Therefore, it is of great interest, yet challenging, to explore suitable anode materials for RIBs with desirable properties.

Opening the layer spacing of graphite and introducing pore defects may be an effective strategy to improve the electrochemical performance of RIB anode material. Porous graphene material with in-plane pores (iPPGs) is a carbon material with nanoscale pores on a two-dimensional surface. Similar to "punching" holes in graphene, which is a functionalized defect of graphene, its pores are empty spaces left by the removal of carbon atoms from the lattice.[20,21] The advantages of iPPGs as an anode material are as follows: (1) weakens the $\pi-\pi$ interactions between graphene sheets and alleviates the stacking problem; (2) provides a larger ion storage space (specific surface area) and enhances the storage of Rb-ions; (3) opens new Rb-ion diffusion channels, which help to accelerate the charging/discharging process and reduce structural deformation, thus enhancing the rate capability and cycling stability;[22] and (4) the new active site formed at the defect can promote the interaction between the anode materials and alkali

metal, which is conducive to high-temperature energy storage. These advantages of iPPGs are often used in alkali-ion electrochemical devices. For example, iPPGs exhibits a high efficiency of Li-ion diffusion and migration when used as an anode material for LIBs, improving the rate capability and cycling stability.[23,24] For SIBs, iPPGs can improve electrolyte accessibility and shorten the diffusion path of Na-ions, thus showing a good reversible capacity.[25] Due to the similarity of energy-storage mechanisms among different monovalent alkali-ion batteries, the strategy of using iPPGs as anode materials in LIBs and SIBs can also be translated to RIBs. Therefore, the iPPGs anode material has good feasibility for improving the electrochemical performance of RIBs.

In this work, based on the properties of the pore structure of iPPGs, we investigated the potential performance of holey graphene (HG) as an anode material for RIBs using first-principles calculations. We built and analyzed three HG systems (HG588, HG1039, and HG1420) with varied pore diameters based on the feasible structures of experimentally synthesized iPPGs. The computational results show that HG1039 not only shows excellent structural stability but also the metallic character of the band structures. When HG1039 is used as the anode in RIBs, very low-ion diffusion energy barriers and high specific capacity may be produced, as well as a low volume change rate during charge/discharge (good cycling stability). In addition, HG1039 and Rb-β-Al$_2$O$_3$ (Rb-ion solid electrolyte) can form a stable interface, which facilitates Rb-ion diffusion. These findings will provide fundamental insights into HG1039 as an ideal anode candidate for RIBs for energy conversion and storage applications.

2. COMPUTATIONAL DETAILS

2.1. Geometric and Electronic Structures. All geometric and electronic structures were studied using DFT calculations by the Vienna ab initio simulation package (VASP).[26,27] We chose the generalized gradient approximation of Perdew, Burke, and Ernzerhof (GGA−PBE)[28] as the exchange−correlation functional with the plane wave basis set to calculate the geometric structures of the HG and HGH systems. Van der Waals interactions were corrected by using the DFT-D3 (Grimme) approach in all systems.[29,30] The cut-off energy was set to 450 eV. The Brillouin zone was regulated with a grid spacing of about $2\pi \times 0.03$ Å^{-1} of k-point meshes for all HG and HGH systems. It is worth noting that the electronic properties of all systems containing heavy metal elements (Rb) are considered to include the spin−orbital-coupling calculation. All geometry structures were fully relaxed until the convergence criteria of energy (10^{-5} eV) and force (0.02 eV/Å) were satisfied. The climbing image-nudged elastic band method was also implemented in the VASP transition state tools to calculate the diffusion barriers of Rb-ions.[31] The periodic boundary condition was applied to minimize the edge effect in a finite system. Vacuum space with at least 20 Å was constructed perpendicular to the layer plane of each HG and HGH system. Please refer to the calculation method of Rb-β-Al$_2$O$_3$ and HG1039@Rb-β-Al$_2$O$_3$ in the Supporting Information.

2.2. AIMD Simulations. All ab initio molecular dynamics (AIMD) simulations were carried out under the *NVT* ensemble. The temperature was controlled by the weak coupling of a Nosé−Hoover thermostat.[32] The snapshots were saved in time intervals of 2 fs (timestep was set to 2 fs) to collect data for analysis at 400 K. It is important to note that

the duration of AIMD is set according to the atomic number of the system to improve the cost effectiveness of the calculation, that is, the simulation duration of HG, HGH, and HG1039@Rb-β-Al$_2$O$_3$ systems was 20 ps and that for Rb$_n$@HG588, Rb$_n$@HG1039, and Rb$_n$@HG1420 was 10 ps. The probability density of ion migration was obtained by the Pymatgen code.[33]

From the obtained trajectory of the AIMD simulation, the mean square displacement (MSD) was calculated by eq 1 for Rb-ions

$$\text{MSD}(\Delta t) = \sum_{i=1}^{N} \frac{1}{N_{\Delta t}} \sum_{t=0}^{t_{\text{tot}}-\Delta t} |r_i(t + \Delta t) - r_i(t)|^2 \tag{1}$$

where r_i is the trajectory of the Rb-ion; $N_{\Delta t}$ is the total number of time intervals Δt during the duration t_{tot} of AIMD. The diffusion coefficient (D) of Rb-ion in the structure can be obtained from the Einstein relation

$$D = \frac{1}{N} \frac{\text{MSD}(\Delta t)}{2d\Delta t} \tag{2}$$

where d is the dimension (here, d is 3); N is the number of Rb-ions.

3. RESULTS AND DISCUSSION

3.1. Geometry Structure and Stability. Pore engineering in the graphene structure yields the structure of iPPGs, which possesses both graphene and porous material features. Here, we make an iPPGs model based on the physical characteristics of previous experiment studies, paying special attention to the following: (1) the introduced hole originates from an equilateral hexagonal defect in the C atom (Figure 1a). Previous research has demonstrated that introducing a sequence of pores with equilateral hexagonal defects on the graphene surface is not only simple to do experimentally but also has higher thermodynamic stability than other shaped holes. (2) The pore size ranges from 5 to 15 Å and the pore spacing is greater than 5 Å. The pore size should not only allow at least one Rb atom (∼5 Å diameter) to pass smoothly, but also the pore size control within 15 Å is beneficial to reduce the model size and improve the cost efficiency of the calculation process. The correct pore spacing is important for ensuring structural stability and flatness of iPPGs, increasing tap density, and improving volumetric power and energy density,[20] and thus it needs to be greater than 5 Å. Importantly, the existing techniques are fully capable of ensuring the experimental realization of the above pore size and pore spacing; for example, organic synthesis and chemical etching methods have been used to synthesize iPPGs that satisfy the above mentioned conditions of pore size (single atom width to ∼1 nm) and pore spacing (>7 Å) conditions for iPPGs.[34−36] Based on the aforementioned characteristics, we created three distinct pore size defects to simulate iPPGs, 5.88, 10.39, and 14.20 Å, starting with a perfect graphene structure in an orthorhombic lattice, and their pore spacings are all >7 Å (as shown in Figure 1). Among them, the iPPGs with pink defect (Figure 1a) is named HG588, "HG" stands for HG, and "588" means its pore size is 5.88 Å (Figure 1c). Similarly, the yellow defect and green defect systems are designated as HG1039 (Figure 1f) and HG1420 (Figure 1i), respectively. In addition, we also considered the case of passivation of hydrogen atoms of all dangling bonds at the hole edge positions (i.e., HGH systems). Please refer to the Supporting
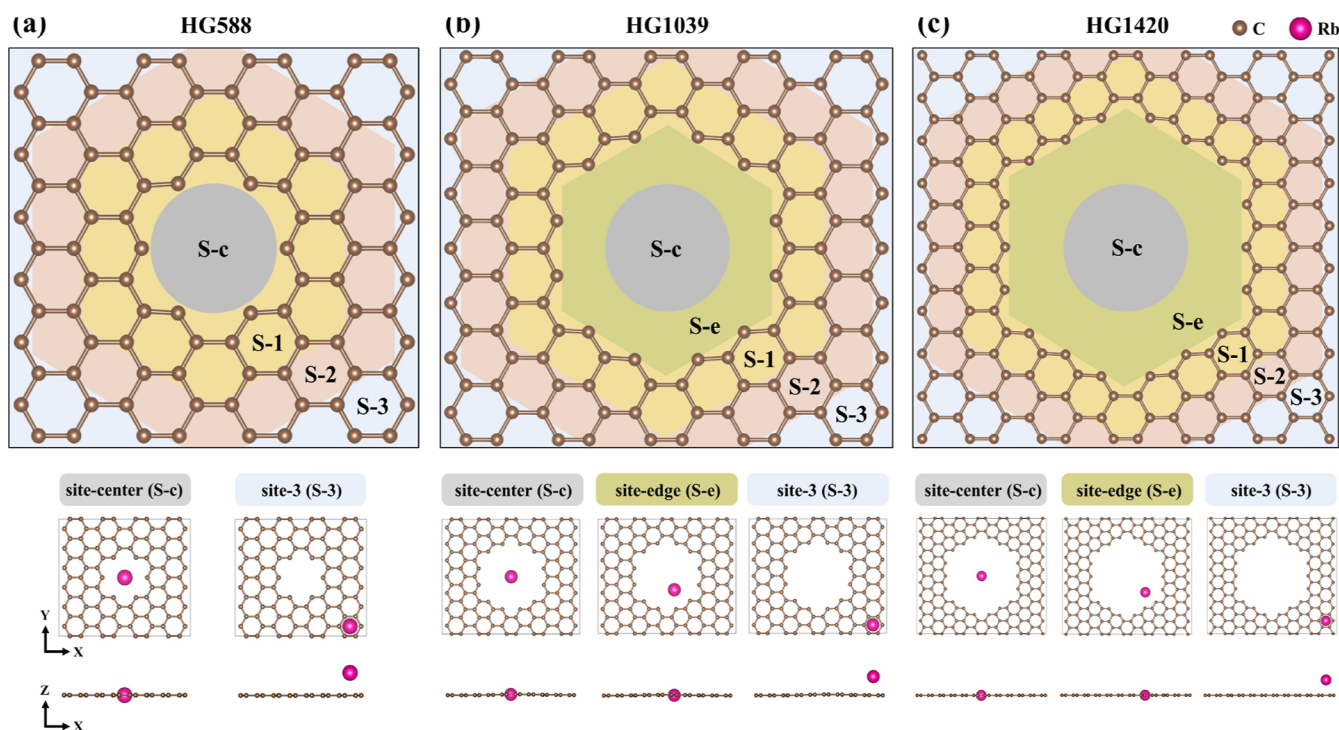
Figure 2. Adsorption sites of Rb atom in (a) HG588, (b) HG1039, and (c) HG1420. The gray, grass-green, yellow, red, and blue areas indicate site-center, site-edge, site-1, site-2, and site-3 adsorption sites, respectively. The top ($x-y$ plane) and front ($x-z$ plane) views of the structure of each system with Rb atoms adsorbed at different adsorption sites are listed below. The brown and pink balls represent C and Rb atoms, respectively.

Information for the structural parameters of HG and HGH and the adsorption properties of HGH.

The HG systems retain their original structure and have high static stability after sufficient structural optimization. Here, we used AIMD simulations with a total simulation time of 20 ps to calculate the stability of HG at 400 K. During the AIMD simulations of the HG systems, the energies of the HG588, HG1039, and HG1420 systems all oscillate only slightly at the equilibrium position with energy fluctuations in the range of 0.04–0.05 eV per atom (Figure 1b,e,h). Especially, at 20 ps, their structural integrity is well maintained, with negligible distortion in the $x-y$ plane and just little displacement in the z direction (Figure 1d,g,j). Therefore, HG588, HG1039, and HG1420 show high thermodynamic stability.

3.2. Adsorption of Rb Atoms. *3.2.1. Stability of a Single Rb Atom Adsorbed on HG Systems.* The identification of Rb atom adsorption sites on HG systems is significant for assessing the possible electrochemical characteristics of HG systems. $Rb_n@HG$ is the structure formed by Rb atoms being adsorbed on HG (n denotes the number of Rb). We discovered five probable adsorption sites based on the symmetry of the HG structure (Figure 2): the site-edge adsorption site (green area) is located at the pore edge; the site-center adsorption site (gray area) is located in the pore center, the honeycomb structure adjacent to the pore is the site-1 adsorption site (yellow area), followed by the site-2 adsorption site (red area), and the other areas are the site-3 adsorption site (blue area). The site's adsorption activity was calculated using the adsorption energy (E_{ad})

$$E_{ad} = \frac{E_{Rb@HG} - E_{HG} - nE_{Rb}}{n} \qquad (3)$$

where $E_{Rb@HG}$, E_{HG}, and E_{Rb} are the total energy of the HG systems with Rb-adsorbed, the energy of HG systems, and the energy of Rb metal, respectively. And n represents the number of Rb atoms adsorbed in the HG systems. E_{ad} values in the negative range indicate more stable adsorption, faster atom loading procedures, and a high potential for alkali metal storage applications. Figure 2 and Table S1 show the adsorption structure and E_{ad} of Rb atoms. Site-edge is the best adsorption site for HG588, HG1039, and HG1420, with E_{ad} values as high as −2.51, −2.17, and −2.25 eV, respectively (site-center and site-edge for HG588 are equivalent). We discovered two intriguing phenomena: the first observation is that as the pore size of the HG systems increases (i.e., 5.88, 10.39, and 14.20 Å), the adsorption energy of Rb at the site-center significantly decreases (with values of −2.51, −1.23, and −0.30 eV, respectively); the second is that the Rb atoms adsorbed on site-1 and site-2 will move toward the pore direction during geometry optimization and eventually stabilize on site-edge (for the surface adsorption sites, we only consider the hollow site of the honeycomb structure, which is due to the positive E_{ad} values of the C-top and C-bridge site; the findings are shown in Table S2).

To explore the charge-transfer phenomenon, we calculated the difference in charge density ($\Delta\rho$) and the Bader charge to better understand the interaction between Rb atoms and the HG systems. $\Delta\rho$ is defined as follows

$$\Delta\rho = \rho_{Rb@HG} - \rho_{Rb} - \rho_{HG} \qquad (4)$$

where $\rho_{Rb@HG}$, ρ_{HG}, and ρ_{Rb} are the charge density values of the HG systems with Rb-adsorbed, HG systems, and Rb atom, respectively. When Rb atom is adsorbed at the site-edge position of the HG system, there is electron depletion from Rb atom, whereas electron accumulation between Rb atom and C
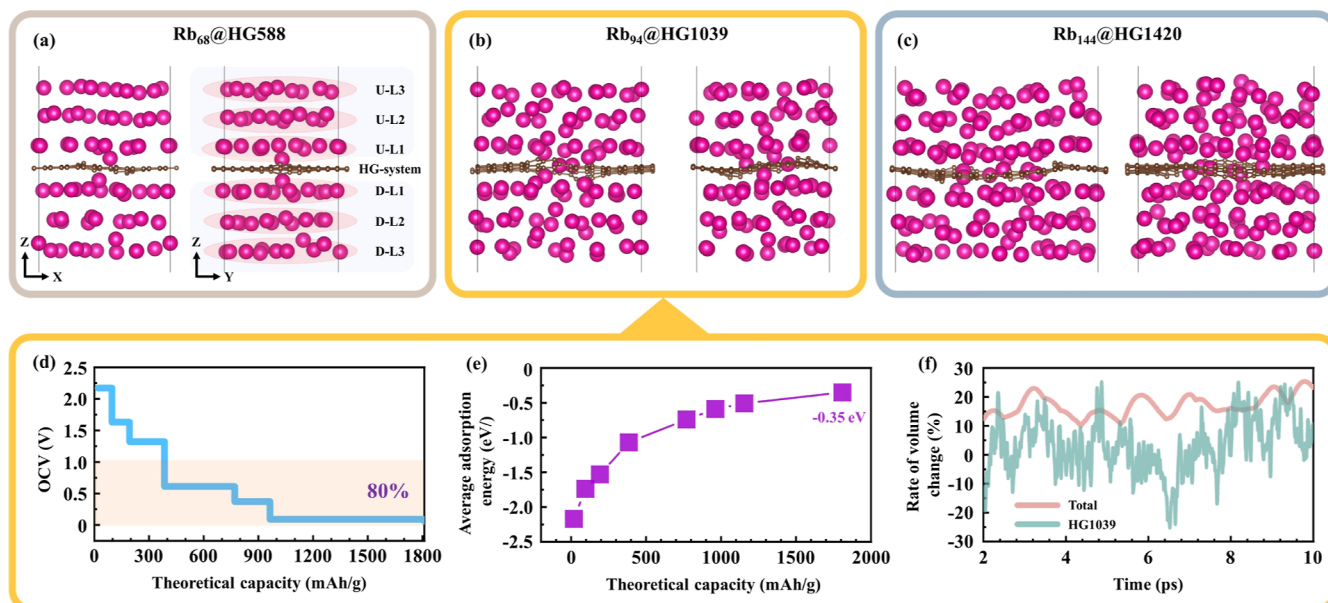
Figure 3. Geometrically optimized structures of (a) Rb_{68}@HG588, (b) Rb_{94}@HG1039, and (c) Rb_{144}@HG1420. (d) Voltage profiles as a function of the Rb-ion storage of Rb_{94}@HG1039. (e) Average adsorption energy as a function of Rb-ion storage in Rb_{94}@HG1039. (f) Volume change rates of Rb_{94}@HG1039 (green line) and HG1039 (light red line, in which Rb_{94}@HG1039) evolves with time at 400 K.
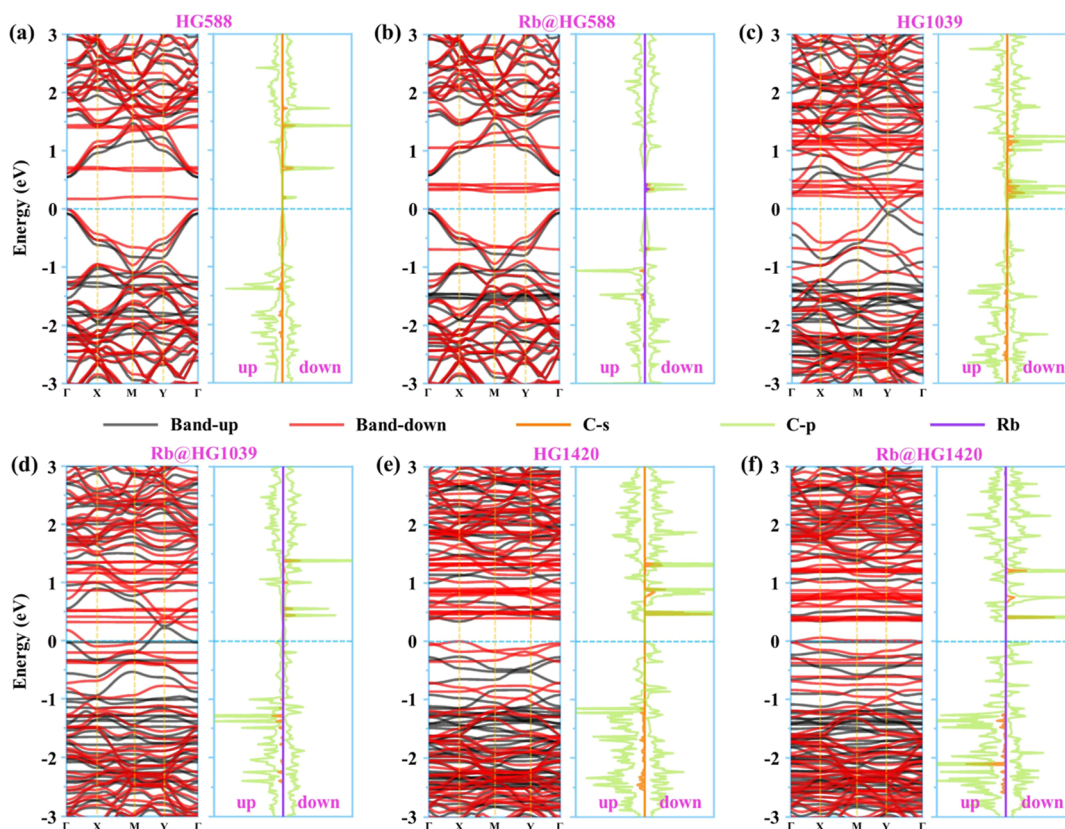
Figure 4. Band structures and PDOS of (a) HG588, (b) Rb@HG588, (c) HG1039, (d) Rb@HG1039, (e) HG1420, and (f) Rb@HG1420. The blue dashed line is the Fermi level, which is set to zero.

atom with a dangling bond (see Figure S3). Also, the computed Bader charges (Table S3) reveal that electrons are transported from Rb atom to HG at all adsorption sites. The results of $\Delta\rho$ and Bader charges coincide, so in the system of Rb@HG, Rb is the electron donor and resides in the Rb ionic state.

The electron localization function (ELF, depicted in Figure S4) displays the electron distribution of HG systems. While the electrons of C atoms on the surface are primarily in the electron gas distribution (ELF value is 0.5), it appears that the electrons are distributed locally at the C dangling bond (ELF value is 0.86). As a result, the positively charged Rb-ion can

interact more strongly with the electronically more localized C dangling bond. This can well explain the two aforementioned phenomena: first, the large pore size lengthens the distance between the C atom with dangling bond and site-center, weakening the Coulomb interaction and causing the adsorption energy to decrease. Second, because site-1 and site-2 are too close to the pore, the strong Coulomb interaction between Rb-ion and the C atom with the dangling bond prevents Rb-ion from adsorbing stably to site-1 and site-2, so that the final adsorption of Rb-ion occurs at site-edge where the electrons are more localized. It can be speculated that the site-center will not be able to adsorb Rb-ion stably as the pore size increases. Therefore, a pore size that is too large will waste useful adsorption area and make it difficult for the anode material to store Rb-ion. However, Rb-ion transport will be hampered by too tiny pores. On balance, HG1039 with suitable site-center adsorption energy and pore size may be a good choice for adsorption of low concentrations of Rb-ion.

3.2.2. Maximum Rb-Ion Storage. The HG system has outstanding adsorption performance for a single Rb-ion, and in this section, we will investigate the maximum storage quantity of Rb-ions for HG systems. Because Rb-atom sources are the primary application of RIBs, the operating temperature of 400 K remains one of the elements to consider in order to expedite Rb release.[12] Here, we utilized AIMD simulations to calculate the maximum Rb-ion adsorption for the HG systems as follows: (1) An adsorption model for the Rb_n@HG system was constructed. Four layers of Rb-ion were adsorbed in the HG material's z-axis direction at the top and bottom, respectively (refer to Figure 3a, each layer is called U-Ln and D-Ln, and n is the layer number), and these Rb-ions were arranged in hexagonal closest packed arrangement. (2) AIMD simulations (400 K, 10 ps) were performed for Rb_n@HG systems with varying Rb-ion adsorption amounts. When the HG systems adsorbed a total of eight layers of Rb-ions, it was discovered that the outermost Rb-ions (i.e., U-L4 and D-L4) would desorb and diffuse rapidly to vacuum within 100 fs, suggesting an excess of adsorbed Rb-ion. The quantity of adsorbed Rb-ion was then gradually lowered until the AIMD simulation results were steady. (3) The maximum adsorption structures of HG systems were Rb_{68}@HG588, Rb_{94}@HG1039, and Rb_{144}@HG1420. For example, when the adsorbed amount of HG is Rb_{74}@HG588, Rb_{104}@HG1039, and Rb_{151}@HG1420, there are still a few Rb-ions desorbed in the outermost layer (Figure S5). Until the concentrations of Rb-ions adsorbed by HG systems are Rb_{68}@HG588, Rb_{94}@HG1039, and Rb_{144}@HG1420, it can be stable throughout the AIMD simulation. Figure S6a−c shows the structures of Rb_{68}@HG588, Rb_{94}@HG1039, and Rb_{144}@HG1420 at 10 ps, respectively, and it is clear that all Rb-ions are stably adsorbed on HG. They have energy variations of just 0.02 eV/atom (Figure S6d), which is even lower than for the pure HG systems (0.04−0.05 eV/atom). Therefore, Rb_{68}@HG588, Rb_{94}@HG1039, and Rb_{144}@HG1420 have the highest Rb-ion adsorption capacity in the HG system.

Here, we optimize the structures of Rb_{68}@HG588, Rb_{94}@HG1039, and Rb_{144}@HG1420 at 10 ps to determine the average E_{ad} (by eq 1), and the optimized structures are displayed in Figure 4a−c, respectively. Interestingly, the average E_{ad} and adsorption densities of Rb_{68}@HG588, Rb_{94}@HG1039, and Rb_{144}@HG1420 are almost identical, with values of −0.35 eV and 0.25−0.27 atom/Å^2 (Table S4), respectively, showing that the maximal Rb-ion adsorption

capacities of the three HG systems are the same. One probable explanation is because they have similar electron distributions, that is, their ELF is almost equal (Figure S4). Importantly, the adsorption densities of Rb_{68}@HG588, Rb_{94}@HG1039, and Rb_{144}@HG1420 are 25−27 times greater than the graphene storage Rb density[11] (i.e., Rb@graphene, 0.01 atom/Å^2). The excellent adsorption density and average E_{ad} indicate that the in-plane pore strategy can effectively enhance the Rb-ion storage.

Theoretical capacity is a critical performance characteristic of anode materials that primarily influences battery features such as energy-storage capacity, open-circuit voltage (OCV), and adsorption density. The theoretical maximum Rb-ion storage (C_{max})[37−39] for the anode is defined by the maximum Rb adsorption capacity by the following equation

$$C_{max} = \frac{1}{M} \times z \times N_{max} \times F \tag{5}$$

where N_{max} represents the maximum adsorption capacity of Rb-ions; z is the valence number of the metal atoms ($z = 1$ for Rb-ion); M is the atomic molar weight of HG systems; and F is the Faraday constant (26,801 mA h/mol). A Li to C atom ratio of 1:6 (i.e., Li_1@C_6) is a generally recognized notion for graphite anodes of commercial LIBs,[39−41] and the maximum theoretical capacity of Li_1@C_6 calculated by eq 5 is 372 mA h/g, which is in perfect accord with the experimental measurement.[41] With the same method, the calculated theoretical maximum Rb-ion storages are 1687, 1810, and 1985 mA h/g for HG588, HG1039, and HG1420, respectively, as shown in Table S3. Since the Rb adsorption densities of HG588, HG1039, and HG1420 are relatively similar, the variation in theoretical capacity is due to the differing Rb/C atomic ratios (0.76, 0.81, and 0.88, respectively). Remarkably, Rb_{68}@HG588, Rb_{94}@HG1039, and Rb_{144}@HG1420 have theoretical capacities (in Table S4) 4−5 times more than Li_1@C_6, and even 24−28 times greater than Rb@graphene (Rb_1@C_{32}). Therefore, the in-plane hole strategy is a promising approach to achieve higher Rb-ion storage capacity.

3.3. Electron Conductivity of HG Systems. Excellent electronic conductivity is a significant indicator of the rate capability of anode materials.[42] Commonly, the introduction of in-plane holes breaks the $\pi−\pi$ conjugation of graphene, leading to a reduction in electronic conductivity.[20] To study the conductivity of HG systems, we calculated band structures and density of states (DOS). As shown in Figure 4, both the HG588 and HG1420 systems have band gaps (near the Fermi energy level), and their band gaps do not seem to decrease even after the Rb-ions adsorption, indicating poor electrical conductivity. The DOS results show that the C 2p orbital plays a decisive role in the distribution of energy levels, and the Rb energy level has almost no contribution near the Fermi energy level, hence HG588 and HG1420 cannot improve the electrical conductivity even after the adsorption of Rb. Obviously, because of the continuous distribution of energy levels in the energy interval near the Fermi energy level, HG1039 displays obvious conductivity (i.e., no band gap). Notice that Rb adsorption had no effect on the electronic properties of HG systems, implying an ionic rather than a covalent interaction between Rb and HG materials, which is consistent with the findings of $\Delta\rho$ and Bader charges. Due to the possible good electrical conductivity of HG1039 and properties of the subsequent anode materials, we only take HG1039 as the object of study.
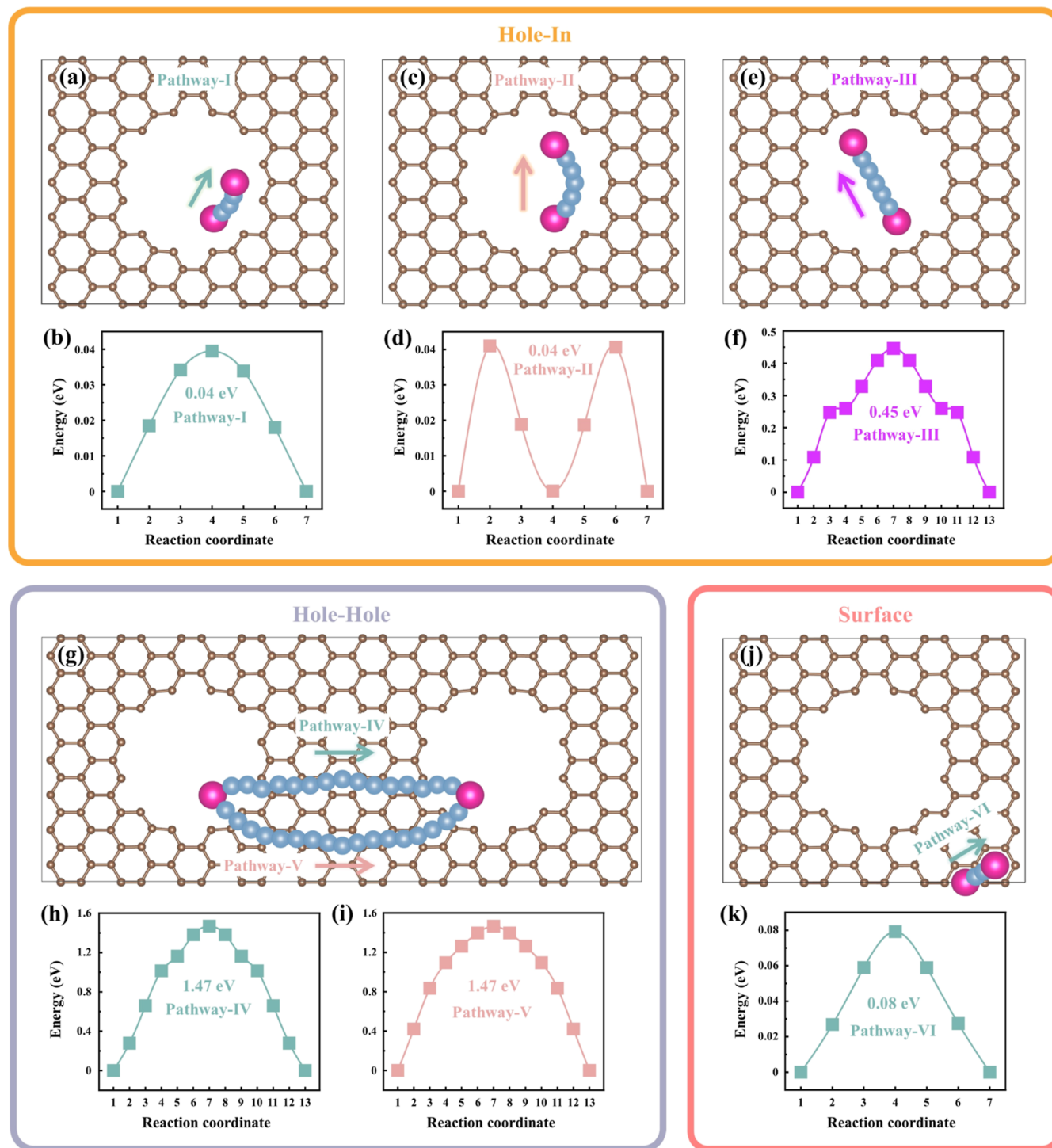
Figure 5. Rb-ion diffusion pathway of (a) pathway-I (ortho-position of hole-in type), (c) pathway-II (meta-position of hole-in type), (e) pathway-III (para-position of hole-in type), (g) pathway-IV and pathway-V of hole−hole type, and (j) pathway-VI of surface type on HG1039. The diffusion energy curves of (b) pathway-I, (d) pathway-II, (f) pathway-III, (h) pathway-IV, (i) pathway-V, and (k) pathway-VI.

3.4. OCV of Rb-Ion on HG1039. An appropriate OCV for the anode material not only facilitates the avoidance of dendrites and metal plating but also aids in increasing energy density.[43] The OCV values for all theoretical capacity intervals were obtained by calculating from the differential adsorption energy. When we ignore the pressure, volume, and entropy effects, the average voltage in the concentration range of $n_1 < n < n_2$ can be calculated as

$$V \approx \frac{E_{Rb_{n1}@HG1039} - E_{Rb_{n2}@HG1039} + (n_2 - n_1)E_{Rb}}{(n_2 - n_1)e} \quad (6)$$

where $E_{Rb_{n1}@HG1039}$ and $E_{Rb_{n2}@HG1039}$ are the total energy of $Rb_{n1}@HG1039$ and $Rb_{n2}@HG1039$, respectively, E_{Rb} is the average energy per Rb atom in the metal, and n_1 and n_2 are the numbers of Rb-ions adsorbed in HG1039. The relationship between OCV and theoretical capacity is shown in Figure 3d
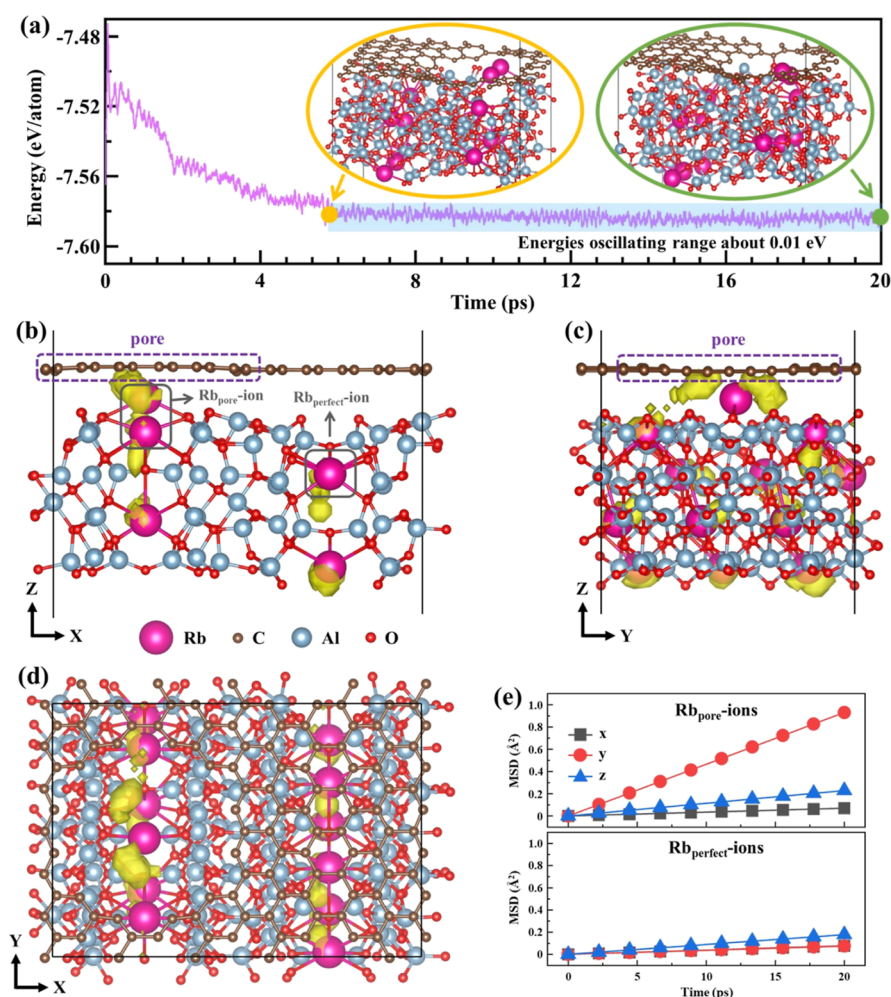
Figure 6. Evolution of total energy per atom of (a) HG1039@Rb-β-Al$_2$O$_3$, the insets in yellow and green borders are snapshots of the structure at 5.8 and 20 ps, respectively. The optimized structure of HG1039@ Rb-β-Al$_2$O$_3$ with Rb-ion probability densities in the (b) $x-z$ plane, (c) $y-z$ plane, and (d) $x-y$ plane. The yellow area indicates the Rb-ion migration probability density with 0.001 e/A^3 isosurface. (e) MSD-fitted line of Rb$_{pore}$-ion and Rb$_{perfect}$-ion. The pink, brown, cyan, and red balls represent Rb, C, Al, and O atoms, respectively.

and Table S5. As theoretical capacity increased, the OCV of HG1039 showed a decreasing trend. This is strongly connected to the average E_{ad}, which decreases with increasing theoretical capacity, as illustrated in Figure 3e. This is because as the number of metal cations increases, so does the repulsive force between them, making Rb-ion at high capacity more readily lower voltage-driven. Furthermore, since no OCV for RIBs has been reported, here we refer to the recommended OCV range for LIBs anode materials, which is <1.0 V.[40] Despite the fact that the OCV range of HG1039 ranges from 0.06 to 2.17 V across the capacity interval, the theoretical capacity interval compatible with an OCV of <1.0 V is 385–1810 mA h/g, approaching 80% of the overall capacity. Therefore, the OCV of HG1039 is appropriate for usage as anode materials in RIBs.

3.5. Cycling Stability of HG1039. Cycling stability is affected by structural deformation of the electrode material during charging/discharging. We extracted the volume change rate of Rb$_{94}$@HG1039 in the AIMD simulation (i.e., the volume of AIMD vs the volume of geometry optimization) to verify the cycling stability of HG1039. The volume change rate versus time is shown in Figure 3f. The overall Rb$_{94}$@HG1039 volume is expanding, with a change rate ranging from 10 to 25%. Since HG1039 varies more in the z-axis direction in

Rb$_{94}$@HG1039, the volume of HG1039 alternates between shrinkage (negative value) and expansion with a variation interval of −25 to 25%. According to the above results, the volume of HG1039 changes <25% during the dynamical evolution. The volume expansibility using HG1039 is much smaller compared to the anode materials for LIBs and SIBs, for example, a 400% expansion rate for silicon-based anodes for LIBs,[44] and 259 and 423% expansion rates for tin-based anodes for LIBs and SIBs,[45] respectively. Therefore, the Rb@HG1039 system has reliable stability during the charging/discharging process.

3.6. Properties of Diffusion. *3.6.1. Diffusion of Rb-Ions on HG1039.* The diffusion and migration ability of metal cations on the anode material is closely related to the rate capability of batteries.[46,47] The lower the diffusion barrier, the faster the metal cations migrate and the better the rate capability of the battery. There are four types of Rb-ion diffusion in the HG1039 system. Diffusion within a pore (hole-in type), diffusion between adjacent pores (hole−hole type), and diffusion on the surface (surface type) are the three cases of monolayer HG1039. In addition, considering that graphene is usually not completely exfoliated in experiments (the case of few-layer), we also considered the fourth case, that is, the

diffusion of Rb-ion within the pores of few-layer HG1039 (layer type). The four cases are as follows:

(i) For hole-in type diffusion (Figure 5a−f), there are three diffusion paths between two site-edge (the most stable) adsorption sites, namely ortho-position (pathway-I), meta-position (pathway-II), and para-position (pathway-III), with corresponding diffusion energy barriers of 0.04, 0.04, and 0.45 eV, respectively. Pathway-I and -II are arc-shaped routes formed around the pore's border, rather than linear diffusion paths. Pathway-II can be thought of as a mixture of two pathway-I. Pathway-III is diffusion along a linear path, and the transition state is site-center. With an energy barrier of only 0.04 eV, ortho-position (pathway-I) is clearly the best diffusion for hole-in type, with an order of magnitude smaller than that of para-position (pathway-III). (ii) For hole−hole type (Figure 5g−i), pathway-IV is relatively shorter than pathway-V (16.58 vs 18.44 Å). Despite the different paths, the diffusion energy barrier of both pathway-IV and -V is 1.47 eV, which is owing to the fact that their transition states are both site-3. (iii) For the surface of HG1039 (surface type), as shown in Figure 5j,k, we calculated the diffusion of two adjacent site-3 (the most stable adsorption site on the surface) adsorption sites. The diffusion path is pathway-VI with a 0.08 eV diffusion energy barrier. (iv) In the case of layer type (Figure S7), the diffusion energy barriers required for Rb-ion in the z-axis direction through site-center and site-edge are 0.12 eV (pathway-VII) and 0.03 eV (pathway-VIII), respectively. Although the diffusion energy barrier of pathway-VIII is only 0.03 eV, the premise of pathway-VIII requires Rb-ion to diffuse from site-edge to site-center (i.e., halfway pathway-III, 0.45 eV energy barrier needs), and the actual total energy barrier of pathway-VIII is 0.48 eV, so pathway-VII is the best choice for Rb-ion interlayer diffusion. Importantly, the diffusion energy barriers of pathway-I, -II, -VI, and -VII are only 0.04, 0.04, 0.08, and 0.12 eV, respectively (data in Table S6), which are substantially lower than those of common energy-storage anode materials, such as Li@graphite (0.45−1.20 eV),[48,49] Li@graphene (0.31−0.48 eV),[50] Li@MoS$_2$ (0.21 eV),[51] Na@MoS$_2$ (0.28 eV),[52] Na@TiC$_3$ (0.18 eV),[37] K@graphite (0.18−0.22 eV),[19] Li/Na/K@C$_2$B (0.75, 0.5, 0.25 eV, respectively),[40] and so forth. These results indicate that HG1039 has excellent Rb-ion transport capacity.

3.6.2. Diffusion of Rb-Ions at the HG1039@Rb-β-Al$_2$O$_3$ Interface. Focusing on electrodes alone is insufficient for developing high-performance RIBs in a variety of operating environments because key reactions and interactions at the electrode−electrolyte interface affect ion alignment and transfer.[1] Here, we built a model of the HG1039@ Rb-β-Al$_2$O$_3$ interface utilizing the electrolyte Rb-β-Al$_2$O$_3$ of RIBs with HG1039 (please refer to the Supporting Information for Rb-β-Al$_2$O$_3$ structure information), and the optimized structure is shown in Figure 6b−d. We named the Rb-ion in β-Al$_2$O$_3$ on the pore side as Rb$_{pore}$-ion, and the Rb-ion in the other side channel corresponding to the perfect structure of graphene as Rb$_{perfect}$-ion. The optimization results demonstrate that the Rb-ion which is not inhibited by HG1039 (i.e., Rb$_{pore}$-ion) prefers to occupy the interface position between HG1039 and Rb-β-Al$_2$O$_3$ (benefiting from the stronger Coulomb interaction between C atoms with a dangling bond and Rb-ion), where the system energy is lowest.

In order to further understand the diffusion behavior of Rb-ions at the interface, AIMD simulations (400 K, 20 ps) were performed for the HG1039@Rb-β-Al$_2$O$_3$ system, and the probability density of ion migration (by Pymatgen code[33]) and diffusion coefficient (by eq 2) were calculated. The energy evolution of the HG1039@Rb-β-Al$_2$O$_3$ system with time is depicted in Figure 6a. The energy of HG1039@Rb-β-Al$_2$O$_3$ begins to fluctuate steadily at 5.8 ps with an oscillation range of only 0.01 eV, which is less than that of both HG1039 and Rb$_{94}$@HG1039. And the structure of HG1039@Rb-β-Al$_2$O$_3$ remains intact at 20 ps, especially the structure of HG1039's pore and β-Al$_2$O$_3$ ion channels are well maintained. This indicates that the HG1039@Rb-β-Al$_2$O$_3$ interface has good stability, which is helpful to the battery's cyclic operation. The probability density of Rb-ion is shown in Figure 6b−d. All of the Rb-ions in the solid electrolyte migrate primarily along the channels in the z-axis direction, whereas the Rb$_{pore}$-ion migrates strongly in the y-axis direction. The y- and z-axes are the major diffusion routes of Rb-ions because the layer-like structure of β-Al$_2$O$_3$ is stacked along the x-axis, resulting in no migration pathways for Rb-ions in the x-axis direction. In addition, the diffusion of Rb$_{pore}$-ion and Rb$_{perfect}$-ion can be utilized to compare the diffusion properties of in-plane pore and perfect graphene structures at the interface. The results of diffusion coefficient (Table S7) and MSD fitting (Figure 6e) show that Rb$_{pore}$-ion has a significant diffusion advantage compared to Rb$_{perfect}$-ion (1.02×10^{-4} vs 2.75×10^{-5} cm^2/s), which is mainly reflected in the migration in the y-axis direction. Therefore, a stable electrode−electrolyte interface can be formed between HG1039 and β-Al$_2$O$_3$, and the interface's improved Rb-ion arrangement and transfer benefits the ion's transport capabilities, making HG1039 a superior RIBs anode material.

4. CONCLUSIONS

In summary, the performance of three in-plane porous graphene systems HG588, HG1039, and HG1420 as anode materials for RIBs was calculated by first-principles calculations. It was demonstrated that HG1039 appears to be the ideal anode material for RIBs with the following outstanding properties: (1) the HG1039 structure is not only thermodynamically stable, but it also has a volume expansion of less than 25% when charging and discharging, which is beneficial to the cycling performance of HG1039-based RIBs. (2) HG1039 accomplishes three-dimensional Rb-ion diffusion with a diffusion energy barrier of just 0.04 eV, which is one order of magnitude lower than that of commercial graphite-based LIBs. And HG1039 and Rb-β-Al$_2$O$_3$ can form a stable electrode−electrolyte interface, which is favorable for the arrangement and transfer of Rb-ions. Furthermore, HG1039 also has good electrical conductivity. As a result, HG1039-based RIBs have exceptional rate capability potential benefits. (3) Because HG1039 has a 26-fold greater Rb-ion adsorption density than graphene, it is more suited for electrochemical Rb atomic sources. (4) The theoretical capacity of HG1039 is up to 1810 mA h/g, which is ~5 times more than that of commercial graphite-based LIBs (372 mA h/g). (5) The physical characteristics of HG1039, such as pore size and pore spacing, are experimentally based and easy for rapid experimental implementation. Therefore, HG1039 with in-plane porous graphene structure is a promising and viable anode material for RIBs.

ASSOCIATED CONTENT

Ⓢ Supporting Information

The Supporting Information is available free of charge at https://pubs.acs.org/doi/10.1021/acsomega.3c01548.

Detailed description for the crystal structures of HG, HGH, and Rb-β-Al$_2$O$_3$ systems; structural stability and adsorption site activity of the HGH systems; calculated parameters for Rb-β-Al$_2$O$_3$ and HG1039@Rb-β-Al$_2$O$_3$; structures of HGH and its Rb adsorption sites; charge density difference; ELF; structures simulated by AIMD; layer-type Rb-ion diffusion pathway; and geometry structure of Rb-β-Al$_2$O$_3$ (PDF)

AUTHOR INFORMATION

Corresponding Author

Jifeng Qu − Center for Advanced Measurement Science, National Institute of Metrology, Beijing 100029, China; Email: qujf@nim.ac.cn

Authors

Baichuan Lu − Center for Advanced Measurement Science, National Institute of Metrology, Beijing 100029, China; ⓞ orcid.org/0000-0002-7477-1065

Ning Ru − Center for Advanced Measurement Science, National Institute of Metrology, Beijing 100029, China

Junyi Duan − Center for Advanced Measurement Science, National Institute of Metrology, Beijing 100029, China

Zesheng Li − Key Laboratory of Cluster Science of Ministry of Education, Beijing Key Laboratory of Photoelectronic/ Electro-Photonic Conversion Materials, School of Chemistry and Chemical Engineering, Beijing Institute of Technology, Beijing 100081, China; ⓞ orcid.org/0000-0002-6993-8414

Complete contact information is available at:
https://pubs.acs.org/10.1021/acsomega.3c01548

Notes

The authors declare no competing financial interest.

ACKNOWLEDGMENTS

REFERENCES

(1) Wang, X.; Salari, M.; Jiang, D.-e.; Chapman Varela, J.; Anasori, B.; Wesolowski, D. J.; Dai, S.; Grinstaff, M. W.; Gogotsi, Y. Electrode material-ionic liquid coupling for electrochemical energy storage. Nat. Rev. Mater. 2020, 5, 787−808.

(2) Nitta, N.; Wu, F.; Lee, J. T.; Yushin, G. Li-ion battery materials: present and future. Mater. Today 2015, 18, 252−264.

(3) Gao, S.; Hao, J.; Zhang, X.; Li, L.; Zhang, C.; Wu, L.; Ma, X.; Lu, P.; Liu, G. Two dimension transition metal boride Y$_2$B$_2$ as a promising anode in Li-ion and Na-ion batteries. Comput. Mater. Sci. 2021, 200, 110776.

(4) Wu, Y.; Huang, H. B.; Feng, Y.; Wu, Z. S.; Yu, Y. The promise and challenge of phosphorus-based composites as anode materials for potassium-ion batteries. Adv. Mater. 2019, 31, 1901414.

(5) Jian, Z.; Luo, W.; Ji, X. Carbon electrodes for K-ion batteries. J. Am. Chem. Soc. 2015, 137, 11566−11569.

(6) Jin, Y.; Le, P. M.; Gao, P.; Xu, Y.; Xiao, B.; Engelhard, M. H.; Cao, X.; Vo, T. D.; Hu, J.; Zhong, L.; et al. Low-solvation electrolytes for high-voltage sodium-ion batteries. Nat. Energy 2022, 7, 718−725.

(7) Lee, S. H.; Rasaiah, J. C. Molecular Dynamics Simulation of Ion Mobility. 2. Alkali Metal and Halide Ions Using the SPC/E Model for Water at 25°C. J. Phys. Chem. 1996, 100, 1420−1425.

(8) Okoshi, M.; Yamada, Y.; Komaba, S.; Yamada, A.; Nakai, H. Theoretical Analysis of Interactions between Potassium Ions and Organic Electrolyte Solvents: A Comparison with Lithium, Sodium, and Magnesium Ions. J. Electrochem. Soc. 2017, 164, A54−A60.

(9) Sultana, I.; Rahman, M. M.; Ramireddy, T.; Chen, Y.; Glushenkov, A. M. High capacity potassium-ion battery anodes based on black phosphorus. J. Mater. Chem. A 2017, 5, 23506−23512.

(10) Biby, A. H.; Ali, B. A.; Allam, N. K. Rb intercalation enhanced the supercapacitive performance of layer-structured MoS$_2$ as a 2D model material. Mater. Adv. 2021, 2, 5052−5056.

(11) Lu, B.; Liu, X.; Qu, J.; Li, Z. Monolayer H-MoS$_2$ with high ion mobility as a promising anode for rubidium (cesium)-ion batteries. Nanoscale Adv. 2022, 4, 3756−3763.

(12) McGilligan, J. P.; Moore, K. R.; Kang, S.; Mott, R.; Mis, A.; Roper, C.; Donley, E. A.; Kitching, J. Dynamic characterization of an alkali-Ion Battery as a source for laser-cooled atoms. Phys. Rev. Appl. 2020, 13, 044038.

(13) Kang, S.; Moore, K. R.; McGilligan, J. P.; Mott, R.; Mis, A.; Roper, C.; Donley, E. A.; Kitching, J. Magneto-optic trap using a reversible, solid-state alkali-metal source. Opt. Lett. 2019, 44, 3002−3005.

(14) Kang, S.; Mott, R. P.; Mis, A. V.; Roper, C. S.; Donley, E. A.; Kitching, J. Active stabilization of alkali-atom vapor density with a solid-state electrochemical alkali-atom source. Opt. Express 2018, 26, 3696−3701.

(15) Kang, S.; Mott, R. P.; Gilmore, K. A.; Sorenson, L. D.; Rakher, M. T.; Donley, E. A.; Kitching, J.; Roper, C. S. A low-power reversible alkali atom source. Appl. Phys. Lett. 2017, 110, 244101.

(16) Rusimova, K. R.; Slavov, D.; Pradaux-Caggiano, F.; Collins, J. T.; Gordeev, S. N.; Carbery, D. R.; Wadsworth, W. J.; Mosley, P. J.; Valev, V. K. Atomic dispensers for thermoplasmonic control of alkali vapor pressure in quantum optical applications. Nat. Commun. 2019, 10, 2328.

(17) Yang, S.-J.; Wang, X.-J.; Bao, X.-H.; Pan, J.-W. An efficient quantum light−matter interface with sub-second lifetime. Nat. Photonics 2016, 10, 381−384.

(18) Lahad, O.; Firstenberg, O. Induced cavities for photonic quantum gates. Phys. Rev. Lett. 2017, 119, 113601.

(19) Ma, J.; Yang, C.; Ma, X.; Liu, S.; Yang, J.; Xu, L.; Gao, J.; Quhe, R.; Sun, X.; Yang, J.; et al. Improvement of alkali metal ion batteries via interlayer engineering of anodes: from graphite to graphene. Nanoscale 2021, 13, 12521−12533.

(20) Tao, Y.; Sui, Z.-Y.; Han, B.-H. Advanced porous graphene materials: from in-plane pore generation to energy storage applications. J. Mater. Chem. A 2020, 8, 6125−6143.

(21) Bai, J.; Zhong, X.; Jiang, S.; Huang, Y.; Duan, X. Graphene nanomesh. Nat. Nanotechnol. 2010, 5, 190−194.

(22) Guo, B.; Yu, X.; Sun, X.-G.; Chi, M.; Qiao, Z.-A.; Liu, J.; Hu, Y.-S.; Yang, X.-Q.; Goodenough, J. B.; Dai, S. A long-life lithium-ion battery with a highly porous TiNb 2 O 7 anode for large-scale electrical energy storage. Energy Environ. Sci. 2014, 7, 2220−2226.

(23) Jiang, Z.; Pei, B.; Manthiram, A. Randomly stacked holey graphene anodes for lithium ion batteries with enhanced electro-chemical performance. J. Mater. Chem. A 2013, 1, 7775−7781.

(24) Zhang, J.; Guo, B.; Yang, Y.; Shen, W.; Wang, Y.; Zhou, X.; Wu, H.; Guo, S. Large scale production of nanoporous graphene sheets and their application in lithium ion battery. Carbon 2015, 84, 469−478.

(25) Luo, X.-F.; Yang, C.-H.; Chang, J.-K. Correlations between electrochemical Na$^+$ storage properties and physiochemical character-istics of holey graphene nanosheets. J. Mater. Chem. A 2015, 3, 17282−17289.

(26) Kresse, G.; Furthmüller, J. Efficient Iterative Schemes for Ab Initio Total-energy Calculations Using a Plane-wave Basis Set. Phys. Rev. B: Condens. Matter Mater. Phys. 1996, 54, 11169−11186.

(27) Kresse, G.; Joubert, D. From Ultrasoft Pseudopotentials to the Projector Augmented-wave Method. *Phys. Rev. B: Condens. Matter Mater. Phys.* **1999**, *59*, 1758−1775.

(28) Perdew, J. P.; Burke, K.; Ernzerhof, M. Generalized Gradient Approximation Made Simple. *Phys. Rev. Lett.* **1996**, *77*, 3865−3868.

(29) Grimme, S.; Antony, J.; Ehrlich, S.; Krieg, H. A Consistent and Accurate Ab Initio Parametrization of Density Functional Dispersion Correction (DFT-D) for the 94 Elements H-Pu. *J. Chem. Phys.* **2010**, *132*, 154104−154122.

(30) Grimme, S.; Ehrlich, S.; Goerigk, L. Effect of the Damping Function in Dispersion Corrected Density Functional Theory. *J. Comput. Chem.* **2011**, *32*, 1456−1465.

(31) Henkelman, G.; Uberuaga, B. P.; Jónsson, H. A climbing image nudged elastic band method for finding saddle points and minimum energy paths. *J. Chem. Phys.* **2000**, *113*, 9901−9904.

(32) Nosé, S. A Unified Formulation of the Constant Temperature Molecular Dynamics Methods. *J. Chem. Phys.* **1984**, *81*, 511−519.

(33) Ong, S. P.; Richards, W. D.; Jain, A.; Hautier, G.; Kocher, M.; Cholia, S.; Gunter, D.; Chevrier, V. L.; Persson, K. A.; Ceder, G. Python Materials Genomics (pymatgen): A robust, open-source python library for materials analysis. *Comput. Mater. Sci.* **2013**, *68*, 314−319.

(34) Bieri, M.; Treier, M.; Cai, J.; Ait-Mansour, K.; Ruffieux, P.; Gröning, O.; Gröning, P.; Kastler, M.; Rieger, R.; Feng, X.; et al. Porous graphenes: two-dimensional polymer synthesis with atomic precision. *Chem. Commun.* **2009**, 6919−6921.

(35) Moreno, C.; Vilas-Varela, M.; Kretz, B.; Garcia-Lekue, A.; Costache, M. V.; Paradinas, M.; Panighel, M.; Ceballos, G.; Valenzuela, S. O.; Peña, D.; et al. Bottom-up synthesis of multifunctional nanoporous graphene. *Science* **2018**, *360*, 199−203.

(36) Zhu, Y.; Murali, S.; Stoller, M. D.; Ganesh, K. J.; Cai, W.; Ferreira, P. J.; Pirkle, A.; Wallace, R. M.; Cychosz, K. A.; Thommes, M.; et al. Carbon-based supercapacitors produced by activation of graphene. *science* **2011**, *332*, 1537−1541.

(37) Yu, T.; Zhao, Z.; Liu, L.; Zhang, S.; Xu, H.; Yang, G. TiC3 monolayer with high specific capacity for sodium-ion batteries. *J. Am. Chem. Soc.* **2018**, *140*, 5962−5968.

(38) Yang, C.; Zhang, X.; Li, J.; Ma, J.; Xu, L.; Yang, J.; Liu, S.; Fang, S.; Li, Y.; Sun, X.; Yang, X.; Pan, F.; Lu, J.; Yu, D. Holey graphite: A promising anode material with ultrahigh storage for lithium-ion battery. *Electrochim. Acta* **2020**, *346*, 136244.

(39) Zhang, X.; Yang, C.; Pan, Y.; Weng, M.; Xu, L.; Liu, S.; Yang, J.; Yan, J.; Li, J.; Shi, B.; et al. Monolayer GaS with high ion mobility and capacity as a promising anode battery material. *J. Mater. Chem. A* **2019**, *7*, 14042−14050.

(40) Ding, Y.; You, C.; Xu, Y.; Zhong, L.; Deng, Q.; Li, J.; Xiao, B. Stability and reaction thermodynamics of boron-doped nitrogenated holey graphene (NHG) monolayers and their energy storage properties for Li, Na and K-ion batteries: A first principles investigation. *Appl. Surf. Sci.* **2021**, *559*, 149849.

(41) Winter, M.; Besenhard, J. O.; Spahr, M. E.; Novak, P. Insertion electrode materials for rechargeable lithium batteries. *Adv. Mater.* **1998**, *10*, 725−763.

(42) Zhou, L.; Tufail, M. K.; Liao, Y.; Ahmad, N.; Yu, P.; Song, T.; Chen, R.; Yang, W. Tailored Carrier Transport Path by Inter-penetrating Networks in Cathode Composite for High Performance All-Solid-State Li-SeS$_2$ Batteries. *Adv. Fiber Mater.* **2022**, *4*, 487−502.

(43) Wu, M.; Xin, B.; Yang, W.; Li, B.; Dong, H.; Cheng, Y.; Wang, W.; Lu, F.; Wang, W.-H.; Liu, H. Metallic Monolayer Ta$_2$CS$_2$: An Anode Candidate for Li$^+$, Na$^+$, K$^+$, and Ca^{2+} Ion Batteries. *ACS Appl. Energy Mater.* **2020**, *3*, 10695−10701.

(44) Chan, C. K.; Peng, H.; Liu, G.; McIlwrath, K.; Zhang, X. F.; Huggins, R. A.; Cui, Y. High-performance lithium battery anodes using silicon nanowires. *Nat. Nanotechnol.* **2008**, *3*, 31−35.

(45) Liang, S.; Cheng, Y. J.; Zhu, J.; Xia, Y.; Müller-Buschbaum, P. A chronicle review of nonsilicon (Sn, Sb, Ge)-based lithium/sodium-ion battery alloying anodes. *Small Methods* **2020**, *4*, 2000218.

(46) Jia, J.; Li, B.; Duan, S.; Cui, Z.; Gao, H. Monolayer MBenes: prediction of anode materials for high-performance lithium/sodium ion batteries. *Nanoscale* **2019**, *11*, 20307−20314.

(47) Zhao, B.; Ren, Z.; Tan, G.; Li, Z.; Xie, J. Defects on Li$_2$S@ graphene cathode improves the performance of lithium-sulfur battery, A theoretical study. *Acta Mater.* **2022**, *226*, 117632.

(48) Thinius, S.; Islam, M. M.; Heitjans, P.; Bredow, T. Theoretical study of Li migration in lithium-graphite intercalation compounds with dispersion-corrected DFT methods. *J. Phys. Chem. C* **2014**, *118*, 2273−2280.

(49) Yazami, R.; Touzain, P. A reversible graphite-lithium negative electrode for electrochemical generators. *J. Power Sources* **1983**, *9*, 365−371.

(50) Toyoura, K.; Koyama, Y.; Kuwabara, A.; Oba, F.; Tanaka, I. First-principles approach to chemical diffusion of lithium atoms in a graphite intercalation compound. *Phys. Rev. B: Condens. Matter Mater. Phys.* **2008**, *78*, 214303.

(51) Chen, X.; He, J.; Srivastava, D.; Li, J. Electrochemical cycling reversibility of LiMoS$_2$ using first-principles calculations. *Appl. Phys. Lett.* **2012**, *100*, 263901.

(52) Mortazavi, M.; Wang, C.; Deng, J.; Shenoy, V. B.; Medhekar, N. V. Ab initio characterization of layered MoS$_2$ as anode for sodium-ion batteries. *J. Power Sources* **2014**, *268*, 279−286.